Food and Chemical Toxicology 131 (2019) 110523

Contents lists available at ScienceDirect

Food and Chemical Toxicology

journal homepage: www.elsevier.com/locate/foodchemtox

Intrinsic relative potency of a series of pyrrolizidine alkaloids characterized by rate and extent of metabolism

Cathy Lester[a,*], John Troutman[a], Cindy Obringer[a], Kenneth Wehmeyer[a], Peter Stoffolano[a], Michael Karb[a], Yan Xu[a], Amy Roe[a], Greg Carr[a], Karen Blackburn[a], Catherine Mahony[b]

[a] Procter & Gamble, Mason Business Center, 8700 Mason - Montgomery Rd, Mason, OH, 45040, USA
[b] Procter & Gamble Technical Centre, Whitehall Lane, Egham, Surrey, TW20 9AW, UK

ARTICLE INFO

Keywords:
Pyrrolizidine alkaloids
DHP
DNA adducts
Sandwich culture hepatocyte
Relative potency factor

ABSTRACT

1,2-Unsaturated pyrrolizidine alkaloids (PAs) are sometimes present in foods or herbal supplements/medicines as impurities and pose potential concerns for liver genotoxicity/carcinogenicity. PAs display a strong structure toxicity relationship, however, current regulatory approaches to risk assessment take the precautionary approach of assuming all PAs display the same potency as the most toxic congeners lasiocarpine (LAS) and riddelliine (RID). Here we explore the relative potencies of a series of structurally diverse PAs by measuring DNA adduct formation *in vitro* in a rat sandwich culture hepatocyte (SCH) cell system. The adducts generated are consistent with those identified *in vivo* as biomarkers of PA exposure and potential liver-tumor formation. DNA reactive PAs require metabolic activation to form intermediates that bind DNA, therefore, adduct formation is a direct reflection of reactive metabolite formation. Since the area under the concentration versus time curve (AUC) for the depletion of parent PA from the extracellular media is a measure of PA exposure, the ratio of adducts/AUC provides a measure of hepatocyte exposure to DNA-binding metabolites corresponding to an intrinsic potency for DNA adduct formation. Intrinsic potencies relative to potencies for LAS compare well with existing relative potency data further affirming that PA toxicity varies considerably with chemical structure.

1. Introduction

The natural occurrence of pyrrolizidine alkaloids (PAs) and their N-Oxides has been described previously in addition to the toxicities associated with their exposure (EFSA, 2017). It is the cancer endpoint that is the driving toxicological endpoint for the risk assessment given the current conservative low dose extrapolation methods adopted by regulatory authorities. Since 1,2-unsaturated PAs that are DNA reactive act via formation of a reactive ester intermediate, current regulatory approaches to risk assessment take a precautionary approach and calculate an additive exposure across PAs assuming all 1,2-unsaturated PAs display the same toxicity as the most potent PAs such as LAS or RID (EFSA, 2011, 2017), the only PAs with traditional cancer bioassay test data. Recently PAs have been proposed to display a strong structure toxicity relationship with relative potencies spanning several orders of magnitude across structural classes (Allemang et al., 2018; Merz and Schrenk, 2016). The differences in relative potency are likely driven by toxicokinetics, rate and extent of metabolic activation and genotoxic potency, with resulting liver tumors being mediated through a common mode of action whereby cytochrome P450 catalyzed metabolic activation results in the formation of a set of four DNA adducts with levels that correlate with liver tumor potency (Xia et al., 2013).

Consisting of a necine base with two alcohol groups esterified to one or two acid groups, the relative potencies of PAs depend not only on the presence of an unsaturated bond between carbon atoms 1 and 2 but also on the absolute configuration of carbon atom 7 and the nature and number of ester bonds. Provisional relative potency factors (pRPF) derived by Merz and Schrenk (2016) and based on a collection of *in vivo* and *in vitro* data are displayed in Fig. 1, with representative congeners for those containing a retronecine or heliotridine base plus one control PA containing a platynecine base. The most potent congener classes include diesters with a 7S configuration and two different molecules with acid groups in an open arrangement (LAS) plus diesters with a 7R configuration esterified with a cyclic diacid moiety (monocrotaline (MCT), RID). Monoesters shown in Fig. 1 consist of esterification of the C9 carbon of the ring, and the more potent congeners possess a 7S

Abbreviations: PA, 1,2-unsaturated pyrrolizidine alkaloid; SCH, sandwich cultured hepatocyte; AUC, area under the concentration versus time curve; pRPF, provisional relative potency factor; DHP, (±)-6,7-dihydro-7-hydroxy-1-hydroxymethyl-5*H*-pyrrolizine; P450, cytochrome P450

* Corresponding author.
E-mail address: lester.cc@pg.com (C. Lester).

https://doi.org/10.1016/j.fct.2019.05.031
Received 12 March 2019; Received in revised form 17 May 2019; Accepted 18 May 2019
Available online 23 May 2019
0278-6915/

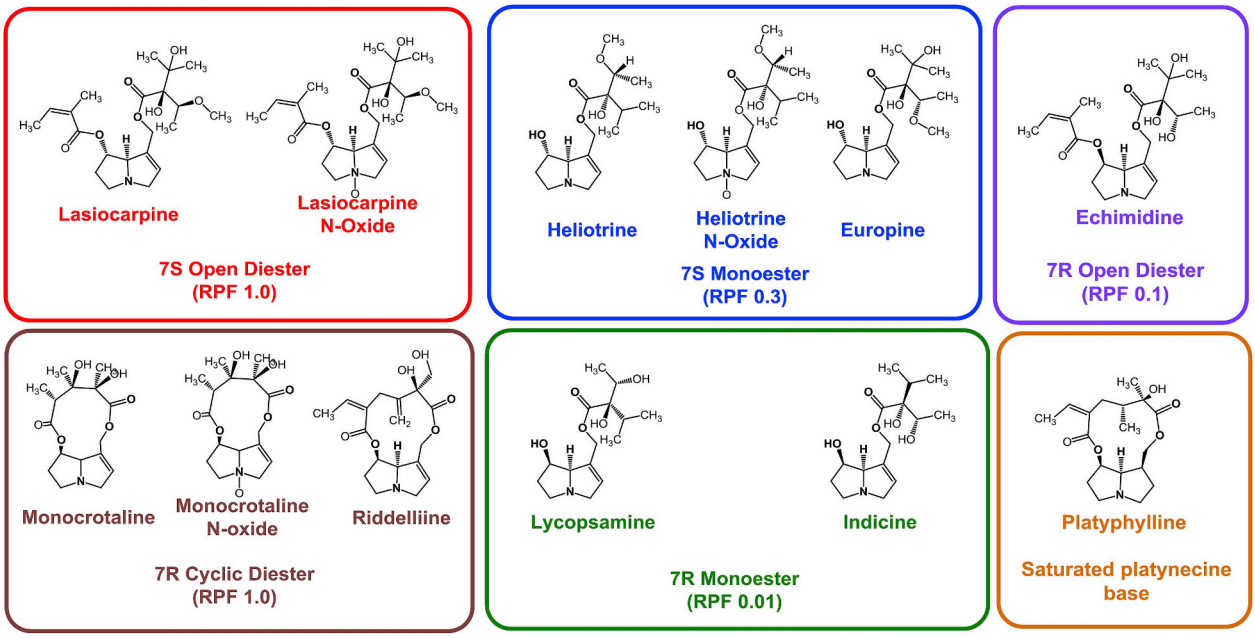

Fig. 1. Chemical structures for 13 PAs, organized by structural configuration and associated interim RPFs determined by Merz and Schrenk (2016).

configuration (heliotrine (HEL), europine (EUR)) with a pRPF of 0.3 followed by a 7R configuration (lycopsamine (LYC) and indicine (IND)) with a pRPF of 0.01. A final congener class consists of an open diester with a 7R configuration (echimidine (ECH)) displaying a pRPF of 0.1 which is an order of magnitude lower than the pRPF for LAS. A representative PA containing a saturated necine base is platyphylline (PLA) that does not interact with cellular macromolecules (Ruan et al., 2014a). Because N-oxidation is a biotransformation present in plants, many plants also contain the N-oxide derivatives of the parent PAs. Some of these structures also are shown in Fig. 1.

Metabolic activation is required for PA toxicity, predominantly driven by CYP3A4 and CYP3A5, except for MCT where CYP2A6 and CYP2E1 play a major role (Ruan et al., 2014b). An understanding of the genotoxic mechanism of liver tumor formation has been developed and involves the formation of PA-derived DNA adducts with the proposed mechanism from Fu (2017) shown in Fig. 2. Bioactivation involves the P450 mediated hydroxylation of the necine base at the C3 or C8 position followed by spontaneous dehydration to produce the reactive (±)-6,7-dihydro-7-hydroxy-1-hydroxymethyl-5H-pyrrolizine ester (pyrrolic ester) intermediate. This intermediate may bind DNA nucleotides with purine bases at the exocyclic nitrogen atom to form the following 4 possible DHP-DNA adducts: epimeric 7-hydroxy-9-(deoxyguanosine-N2-yl)dehydrosupinidine (DHP-dG-3 and DHP-dG-4) and epimeric 7-hydroxy-9-deoxyguanosin-N6-yl)dehydrosupinidine (DHP-dA-3 and DHP-dA-4) (Zhao et al., 2012). These four DHP-DNA adducts have been detected *in vivo* in rats, mice and cattle after exposure to hepatotoxic PAs or PA-Noxides (Fu et al., 2017; Xia et al., 2013; Zhu et al., 2017). The reactive DHP ester intermediate also may react with reduced glutathione (GSH) to form 7-glutathione-DHP, cysteine to form 7-cysteine-DHP or undergo ester bond hydrolysis to produce DHP, forming a set of interconverting secondary metabolites that have been observed *in vivo* and *in vitro* (He et al., 2016). As shown in Fig. 2, both the reactive DHP intermediate and the secondary metabolites can react with DNA to form the same four DHP-DNA adducts. Incubations of reactive DHP ester metabolites dehydroriddelliine, dehydromonocrotaline, dehydroretronecine (DHR, the 7R enantiomer of DHP), 7-glutathione-DHP and 7-cysteine-DHP with human hepatocarcinoma HepG2 cells or human A549 brochoalveolar carcinoma cells also produced the characteristic four DHP-DNA adducts (He et al., 2017, 2019). The formation of other DNA reactive secondary metabolites is possible and has been investigated *in vitro* in the presence of calf thymus DNA or HepG2 cells for a series of O-, N- and S-linked ethers (Xia et al., 2018).

Biotransformations also can detoxify PAs. Possible detoxification transformations also shown in Fig. 2 include ester bond hydrolysis or N-oxidation (Fu et al., 2004). Hydrolysis in the liver is mediated by both microsomal and cytosolic carboxylesterases to hydrolyze ester groups involving C9 and C7 (for diesters), forming the necic acid and corresponding necine base. N-oxidation of retronecine and heliotridine-type PAs was found to be catalyzed by flavin-containing monooxygenases in addition to P450 enzymes with relative reactivities found to be species and tissue dependent.

In addition to metabolic activation and detoxification of PAs, their relative toxicity also may depend on cellular uptake and efflux. MCT and retrorsine (RTS) have been shown to be substrates of organic cation transporter 1 (OCT1) (Tu et al., 2013, 2014) while HEL and ECH have been shown to be actively excreted from the gastrointestinal epithelium to the gut lumen in Madin–Darby canine kidney II/P-glycoprotein (ABCB1)-overexpressing cells (Hessel et al., 2014). Biliary excretion of reactive pyrrolic metabolites also may be important as shown for ^{14}C-labeled MCT in isolated rat liver preparations (Lame et al., 1995).

Based on the premise that all 1,2-unsaturated PAs exhibit toxicity through the same mode of action, we examine here a series of structurally diverse PAs to determine their metabolic stability and ability to form DHP-DNA adducts, providing insight into intrinsic exposure to reactive metabolites and thus informing on a relative ranking of PA potency in the liver. We define this as “intrinsic” potency since the *in vitro* model addresses the ability of the PAs to form DNA adducts in an *in vitro* hepatocyte system which compares potency based on dose to the hepatocytes without the influence of systemic bioavailability and distribution (these factors will be addressed in a subsequent publication). Rat hepatocytes in sandwich culture format are selected for this study because they express transporters and metabolic enzymes consistent with *in vivo* expression while effectively replicating biliary clearance (Swift et al., 2010). These studies represent the first measurement of PA mediated DHP-DNA adducts in a metabolically competent cell system with levels of adduct formation reflecting the proposed range of potencies of PA toxicity and interpreted in terms of the metabolic kinetics.

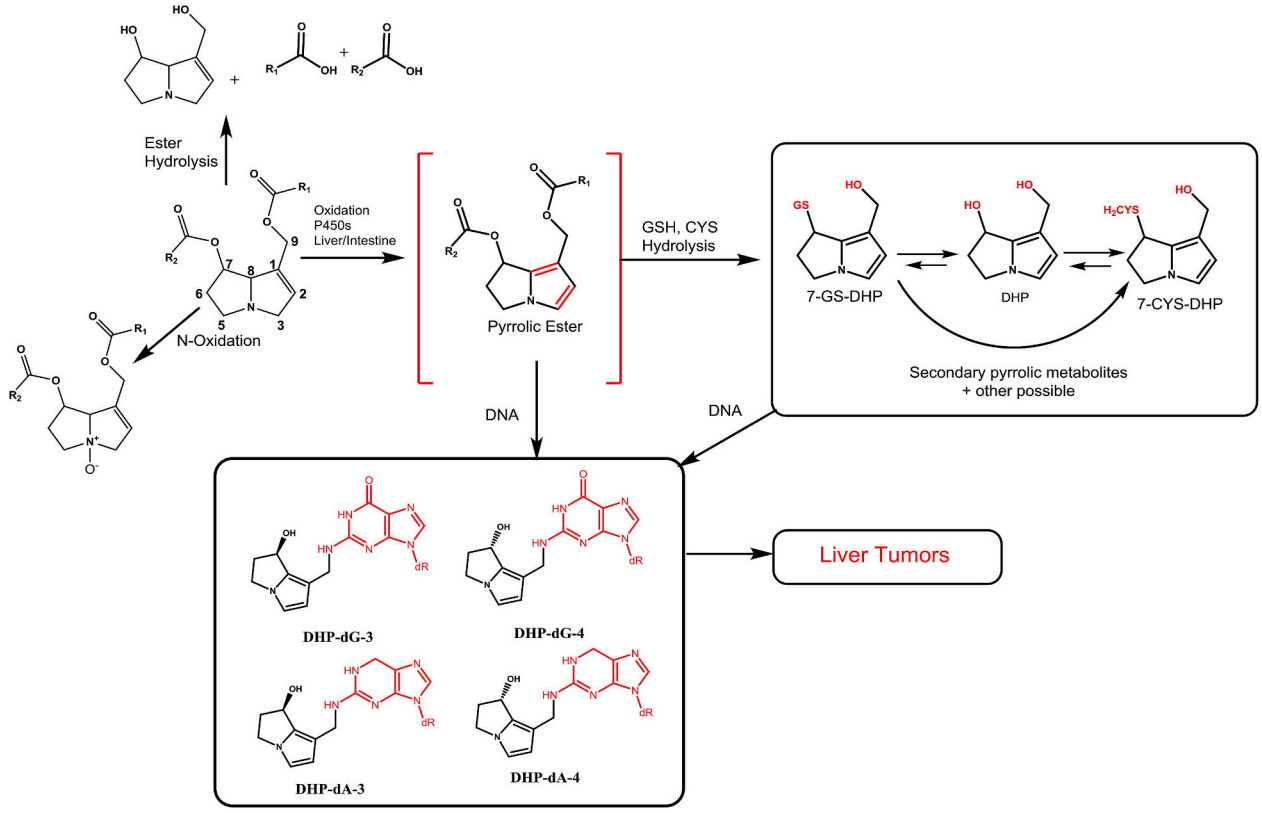

Fig. 2. Proposed scheme for detoxification, activation and DNA adduct formation for a generic PA with an open di-ester configuration where R_1 and R_2 represent the necic acid components.

Using the AUC of the parent PA to reflect hepatocyte exposure and the adduct levels to reflect reactive metabolite formation, we show that the ratio of the # adducts/AUC represents an intrinsic potency of a PA to generate DNA adducts. Consideration of this ratio relative to that for a reference compound such as LAS provides a useful measure of intrinsic relative toxic potential for a series of congeners, and these relative measures of PA hepatotoxicity are compared with the provisional potency factors proposed by Merz and Schrenk (2016).

2. Materials and methods

2.1. Chemicals

All PAs (lasiocarpine, CAS# 303-34-4; heliotrine, CAS# 303-33-3; riddelliine, CAS# 23246-96-0; europine, CAS# 570-19-4; echimidine, CAS# 520-68-3; indicine, CAS# 1195140-94-3; monocrotaline, CAS# 315-22-0; and lycopsamine, CAS# 10285-07-1) were purchased from PhytoLab GmbH & Co. KG. (Vestenbergsgreuth, Germany), except platyphylline (CAS# 480-78-4) which was purchased from Matrix Scientific (Columbia, SC) with chemical structures shown in Fig. 1. Stocks were prepared in methanol at 500X the desired test concentration, resulting in a final methanol concentration of 0.2%.

2.2. Hepatocytes

Male Sprague-Dawley rat sandwich-culture hepatocytes (B-Clear® kits), plated in 24-well format, were purchased from BioIVT (Durham, NC). All culture and assay medias were provided by BioIVT with the B-Clear® kit. BioIVT characterized the transporter function of each SCH kit by evaluating the BSEP (bile salt efflux pump) transporter using ^{3}H-taurocholic acid.

3. Experimental procedure

3.1. DNA adduct formation in rat SCHs

DNA adducts formed by incubating PAs with rat SCHs were measured at substrate concentrations up to 100 μM and incubated for 6 and/or 24 h at 37 °C under 5% CO_2. To isolate enough DNA, an entire 24 well plate (9 x 10^6 cells at a density of 1.25 x 10^6 cells/mL) was pooled and utilized as one replicate (i.e. per compound, concentration, and time point). Along with the DNA adduct measurements in these incubations, the extracellular concentrations of the parent PAs were measured. Initially, additional wells were utilized for CYP450 activity controls, using testosterone at 200 μM and 7-ethoxycoumarin at 500 μM, for up to 4 h. Formation of 6β-hydroxytestosterone and 7-hydroxycoumarin, respectively, were evaluated. Due to further metabolism of the metabolite of interest, the CYP activity control incubation time was reduced to 30 min and the 7-ethoxycoumarin test concentration was reduced to 1 μM to enable monitoring loss of 7-ethoxycoumarin.

Following incubations and removal of media, the plates were washed three times with ice-cold Plus buffer (BioIVT) and aspirated to dryness. The plates were parafilmed, placed in Ziploc® bags, and frozen at −80 °C for at least 24 h or until needed within 1 week. The hepatocytes were lysed and removed from the plate using 70/30 methanol/water. DNA was extracted from the hepatocytes using a Blood and Cell Culture DNA kit (Qiagen) and solubilized with TE buffer. The concentration of DNA (μg/mL) was measured on a NanoVue, which also evaluates the purity of the extracted DNA via the absorbance at 260 nm and 280 nm. The purity of the DNA was checked by measuring the A260/A280 ratio ensuring it falls within the range of 1.7–1.9 (Manchester, 1995). The DNA was hydrolyzed using an EpiQuik One-Step DNA Hydrolysis kit (Epigentek) and analyzed for levels of DHP-DNA adducts via isotope dilution HPLC/MS/MS.

3.2. Quantitation of DHP-DNA adducts

The DHP-dA and DHP-dG adducts, as well as their corresponding stable isotope labeled analogs (DHP[$^{15}N_5$,$^{13}C_{10}$]-dG/A), were prepared from dehydromonocrotaline following the procedure of Zhao (Zhao et al., 2012). Adducts were analyzed by reversed-phase high performance liquid chromatography/tandem mass spectrometry using a system that consisted of a Shimadzu LC20 pump systems, CTC Analytics HTS PAL autosampler and triple quadrupole mass spectrometer Sciex 6500 column. The separation was carried out at ambient temperature on a Waters Atlantis dC18 (2.1 × 150 mm, 3 μm). The mobile phase consisted of water (A) and acetonitrile (B). The flow rate was set to 0.3 mL/min and the injection volume was 20 μL. A gradient elution was programmed as follows: 92% A at 0–5 min, 92-84% A from 5 to 50 min, then to 75% A and held constant 1 min, then back to 99% A from 52 to 60 min to re-equilibrate. The QqQ mass spectrometer was operated under electrospray ionization in the positive mode. The temperature was set to 400 °C with a curtain gas of 30 (nitrogen), ion spray of 5000 V, and declustering potential of 50 V and collision energy was 25 V. Multiple reaction monitoring (MRM) in Analyst 1.6.2 was used to acquire the data with transitions of m/z 403 → 269 DHP-dG and m/z 387 → 253 for DHP-dA. The corresponding stable-isotopically labeled standards were monitored at m/z 418 → 279 DHP-dG and m/z 402 → 263 for DHP-dA.

Standard curves were generated by regression of the peak area ratios (analyte peak area/internal standard peak area) versus quantity of the standard compounds. The levels of DHP-dG-3 and DHP-dG-4 were combined for quantitation; as were the DHP-dA-3 and DHP-dA-4 levels. To each sample and calibration set, a consistent level of DHP [$^{15}N_5$,$^{13}C_{10}$]-dG/A stable labeled internal standard was added. The peak area ratios generated from analysis of the calibration standards were regressed in the instrument software and were weighted quadratic 1/(x*x).

3.3. Substrate depletion assays in rat SCHs

PAs were incubated at 1, 10, and 100 μM with the SCHs to evaluate substrate depletion in the extracellular matrix. Extracellular samples were collected at 1, 2, 3, and 4 h for the 1 μM samples, 0.5, 1, 2, 4 and 6 h for the 10 μM samples and 1,2,3,4 and 24 h for the 100 μM samples and quenched with an equal volume of methanol. Samples were evaluated for the concentration of remaining PA via HPLC/MS/MS.

3.4. In vitro cytotoxicity determinations in male Sprague-Dawley rat hepatocytes

Cytotoxicity was determined by monitoring lactate dehydrogenase (LDH) activity according to the CytoTox-ONE™ Homogenous Membrane Integrity Assay (Promega Corporation, Madison, WI). Briefly, individual PAs were incubated in triplicate wells containing rat SCHs at a target concentration of 100 μM. The incubation conditions were identical to those described for DNA adduct formation (section 2.2.1). Following an incubation period of 24 h, cytotoxicity was determined by measuring the fluorescence (λ_{ex} = 560 nm and λ_{em} = 590 nm) produced from the release of cellular LDH into the culture medium using a SpectraMAX M5 plate reader (Molecular Devices, Sunnyvale, CA). The percentage of cytotoxicity was determined from the ratio of the background corrected average fluorescence from PA cell incubations to the average fluorescence from positive (fully lysed) control cells (LDHMax). Cytotoxicity results are displayed in Table 1. Cell morphology also was examined for evidence of cytotoxicity.

3.5. Analytical methods for quantification of PAs in cell media

Aliquots of extracellular media were analyzed by reversed-phase HPLC-MS/MS analysis using a Sciex Triple Quad 6500 mass spectrometer operating under positive ion electrospray ionization mode with multiple reaction monitoring for detection and quantitation, Shimadzu LC20 pumps and a CTC Analytics HTS PAL autosampler. Chromatography used a Waters Atlantis T3, 3 μm, 2.1 × 100 mm column, with a flow rate of 0.3 mL/min and a gradient of mobile phase A (0.1% formic acid in water + 5 mM ammonium formate) and mobile phase B (0.1% formic acid in methanol + 5 mM ammonium formate). A linear gradient elution program was used as follows: 5% mobile phase B (B) from 0 to 0.5 min, 5–50% B from 0.5 to 3 min, 50–80% B from 3 to 3.6 min, 80–100% B from 3.6 to 4 min with 100% B held constant until 4.8 min, then back to the original conditions (5% B) from 4.8 to 5.4 min, which was held constant until 7.5 min to re-equilibrate the system.

The following compounds were monitored in + MRM mode with precursor and product ions listed: Heliotrine ($[M+H]^+$ m/z 314.1 to m/z 138.1), Lasiocarpine ($[M+H]^+$ m/z 412.2 to m/z 120.1), Riddelliine ($[M+H]^+$ m/z 350.0 to m/z 120.1), Europine ($[M+H]^+$ m/z 330.1 to m/z 138.1), Monocrotaline ($[M+H]^+$ m/z 326.2 to m/z 120.1), Indicine ($[M+H]^+$ m/z 300.2 to m/z 94.0), Lycopsamine ($[M+H]^+$ m/z 300.2 to m/z 94.0), Echimidine ($[M+H]^+$ m/z 398.1 to m/z 120.1), Platyphylline ($[M+H]^+$ m/z 338.2 to m/z 122.0), Senecionine-d3 ($[M+H]^+$ m/z 339.1 to m/z 120.1) and Senecionine N-Oxide-d3 ($[M+H]^+$ m/z 355.1 to m/z 118.1).

Multi-analyte calibration standards (STDs) with quality control check samples (QCs) were used to quantitate analytes in quenched extracellular and intracellular matrix study samples. Deuterated (d_3)-senecionine and (d_3)-senecionine N-oxide were added as internal standards. Specimen concentrations were determined by back-calculation from a weighted ($1/x^2$) quadratic regression of analyte/internal standard peak area ratios to analyte concentrations generated from standards (10–5000 ng/mL). Standards and study specimens were diluted at least 50-fold prior to HPLC-MS/MS analysis.

Table 1
Mean cytotoxicity data following 24 h incubations of 100 μM PAs with male Sprague-Dawley rat sandwich cultured hepatocytes.

Chemical Name	Percent Cytotoxicity		
	Mean	St. Dev.	%CV
Lasiocarpine	2.4	0.4	15
Riddelliine[a]	1.7	–	–
Heliotrine	1.0	0.1	8
Europine	0.6	0.3	44
Monocrotaline	0.6	0.1	11
Echimidine	1.2	0.6	48
Indicine	0.9	0.2	24
Lycopsamine	0.9	0.2	24
Platyphylline	0.6	0.1	18
Untreated	1.0	0.1	9
LDHMax	100	6.7	7

[a] Cytotoxicity for riddelliine was assessed in duplicate wells because the excluded well was inadvertently dosed with cell lysis buffer during the assay.

3.6. Determination of kinetic parameters

In vitro intrinsic clearance (CL_{int}) and half-life ($t_{1/2}$) values for substrate disappearance were determined using the substrate depletion ($t_{1/2}$) approach (Obach, 1999). Briefly, parent substrate concentrations at each timepoint were normalized to the concentration measurement at time zero or to the dosing concentration. The natural log of the percentage remaining versus time at each substrate concentration was used to calculate the first-order depletion rate constant (ke). In cases where the natural log of the substrate remaining versus time plots were nonlinear, only those timepoints where linearity was observed were used to determine depletion rate constants. If substrate depletion was

substantial (> 20% depletion), CL_{int} (Equation (1)) and $t_{1/2}$ (Equation (2)) were calculated from the slope of the natural logarithm of the substrate concentration vs time curve, where the slope equals the first-order depletion rate constant, ke (min^{-1}). In cases where substrate depletion was low (typically < 20% depletion), or in cases where the estimated $t_{1/2}$ was more than 2 times the incubation period, ke and CL_{int} was not reported and $t_{1/2}$ was set equal to a value that was greater than the incubation time.

$$CLint = \frac{ke(min)^{-1}}{million\frac{cells}{mL}} \quad (1)$$

$$t1/2 = \ln(2)/[[ke(min)]]\hat{}(-1) \quad (2)$$

Extracellular AUC calculations: For purposes of comparing time-averaged substrate concentrations to DHP-DNA adduct measurements following 6 and 24 h incubations, the AUC was calculated using the linear trapezoidal rule (Equation (3)), where C_i and C_{i+1} are the substrate concentrations at time t_i and t_{i+1}, respectively. Substrate concentrations at timepoints between zero time and 24 h were calculated using Equation (4). Because kinetic measurements were not determined at the 30 μM substrate concentration, the first-order depletion rate constant for the 30 μM incubation was estimated by non-linear interpolation of the measured values that were determined at substrate concentrations of 1, 10 and 100 μM.

$$AUC_0^t = \sum_{i=0}^{i=n} \frac{(C_i + C_i + 1)}{2} \times (t_i + 1 - t_i) \quad (3)$$

$$C(t) = C_0 * e^{-kt} \quad (4)$$

All calculated values are listed in Table 2.

3.7. Statistical methods

Experimental adducts data (100 μM, 24 hour incubation time) were fit to a linear mixed effects model (Bates et al., 2015). Given that the DNA adducts measurements are count estimates that are all well above zero, and that the sample size is relatively small, the data were subjected to a variance-stabilizing square-root transformation prior to model fitting, and estimates were back-transformed to the measurement scale for reporting and graphical summaries. Individual experimental replicates are treated as a random effect, since two or more chemicals are tested on each batch of cells coming from a single individual. This analysis is conducted in R statistical software (R Core Team, 2018) using the lme4 package.

Table 2
In vitro metabolism kinetic parameters and extracellular AUCs in male Sprague-Dawley rat sandwich cultured hepatocytes.

Chemical Name	Nominal [S] (uM)	ke (min-1)	t1/2 (min)	CLint (uL/min/10^6 cells)	AUC (umol*hr/L) 0–6 h	AUC (umol*hr/L) 0–24 h
Lasiocarpine	1	−0.011	63	8.80	1.71	1.75
LAS	10	−0.0072	96	5.76	22.8	24.7
	30	−0.0048	144	3.84	87.2	105
	100	−0.0023	301	1.84	408	690
Riddelliine	1	−0.0015	462	1.20	4.68	10.1
RID	10	−0.0015	462	1.20	46.5	98.7
	30	−0.0014	495	1.12	142	310
	100	−0.0013	533	1.04	496	1111
Heliotrine	1	−0.0026	267	2.08	3.93	6.3
HEL	10	−0.0013	533	1.04	48.2	110
	30	−0.00094	737	0.752	153	395
	100	−0.00046	1507	0.368	553	1751
Europine	1	NR	> 480	NR	6.0	24
EUR	10	NR	> 720	NR	60	240
	30	NR	> 480	NR	180	720
	100	NR	> 2880	NR	600	2400
Indicine	1	−0.0014	495	1.12	4.72	10.3
IND	10	−0.0010	668	0.830	50.4	127
	30	NR	> 480	NR	180	720
	100	NR	> 2880	NR	600	2400
Monocrotaline	1	NR	> 480	NR	6.0	24
MCT	10	NR	> 720	NR	60	240
	30	NR	> 480	NR	180	720
	100	NR	> 2880	NR	600	2400
Echimidine	1	−0.0042	165	3.36	3.18	4.1
ECH	10	−0.0062	112	4.96	25.1	28.1
	30	−0.0044	158	3.52	92.0	115
	100	−0.0024	289	1.92	404	674
Lycopsamine	1	−0.0013	533	1.04	4.78	10.7
LYC	10	NR	> 720	NR	60	240
	30	NR	> 480	NR	180	720
	100	NR	> 480	NR	600	2400
Platyphylline	1	−0.0053	131	4.24	2.78	3.27
PLA	10	−0.0039	178	3.12	32.7	43.1
	30	−0.0028	248	2.24	115	179
	100	−0.0017	408	1.36	451	904

NR = not reported due to a lack of a well-characterized depletion profile.

4. Results

4.1. Cytotoxicity of PA treated cells

As shown in Table 1, LDH activity in PA treated cells was negligible in comparison to the activity measured in lysed positive control cells. PA-induced cytotoxicity was highest for LAS (2.4%). The percentage of cytotoxicity for the other PAs tested did not exceed 2% of the positive control value.

4.2. Substrate depletion kinetics

Metabolic clearance was determined for all PAs by monitoring the depletion of substrate in the SCH incubation media as a function of time and concentration. These data are presented in Fig. 3 where the % of parent remaining is plotted as a function of incubation time for dose concentrations of 1, 10 and 100 μM with elimination rate constants (k_e), half-lives ($t_{1/2}$), intrinsic clearance values (CL_{int}) and AUCs listed in Table 2. As shown in the figure and in Table 2, the rate and extent of substrate depletion is very much PA dependent. For all concentrations, LAS is the most rapidly metabolized with almost complete loss of parent at incubation times of 4, 6 and 24 h for the 1, 10 and 100 μM samples, respectively. ECH and PLA are depleted almost at the same rate as LAS, particularly for the 100 μM samples where the 0.5–4 h data points for ECH fall on the same curve as LAS with almost equal k_es. At dosing concentrations of 1 and 10 μM, HEL and RID display similar substrate depletion profiles and k_es. At 100 μM, RID is depleted at a faster rate than HEL. At all concentrations, MCT and EUR display the least depletion of parent over the time periods considered. For the slower metabolized PAs, only LYC at a substrate concentration of 1 μM and IND at concentrations of 1 and 10 μM displayed enough depletion for fitting.

As shown in Table 2, the AUC reflects the substrate depletion kinetics. At the lower concentrations of 1 and 10 μM, LAS is almost completely depleted after 4 h resulting in approximately equal AUC for the 6 and 24 h incubations, respectively. ECH and PLA also display similar AUC values for the 6 and 24 h incubations at these lower concentrations. As the rate of metabolism decreases, the difference in AUC for these two time points for a single PA increases. RID and HEL display similar depletion profiles and AUCs at the lower concentrations of 1 and 10 μM, however at 100 μM, the depletion profiles are similar up to the 6 h incubation time displaying similar AUCs at this time point, but diverge at the later time points as reflected in the very different 24 h AUCs. The slowly metabolized PAs EUR, IND, MCT and LYC display little substrate depletionwith AUC values showing little or no substrate loss over the incubation times considered here.

4.3. DHP-DNA adduct measurements

Levels of DHP-DNA adducts identified in the rat SCH cell model and expressed as number of adducts in 10^8 nucleotides (nt) are presented in Fig. 4 with values listed in Table 3. The four adducts identified are consistent with those observed *in vivo* and *in vitro* in cell systems ((Fu et al., 2017; He et al., 2017; Xia et al., 2013; Zhu et al., 2017). Total adduct levels are displayed for each independent study corresponding to hepatocytes from a single rat and for a given PA after a 24 or 6 h incubation at a dosing concentration of 100 μM. Relative adduct levels for each PA can be compared within a single study, where the greatest number of adducts are generated by LAS, HEL, RID and ECH with fewer adducts observed for EUR, MCT, LYC and IND for both incubation times. No adducts were detected for PLA which contains a saturated necine base. Study number 6 involved the incubation of eight PAs using hepatocytes from a single source with a 6 h incubation time and a dosing concentration of 100 μM. Under these conditions, LAS is only ~60% depleted and forms levels of adducts that are significantly higher than levels for the other PAs. Higher levels were evident for HEL, RID and ECH with lower levels for the more slowly metabolized PAs EUR, MCT, LYC and IND.

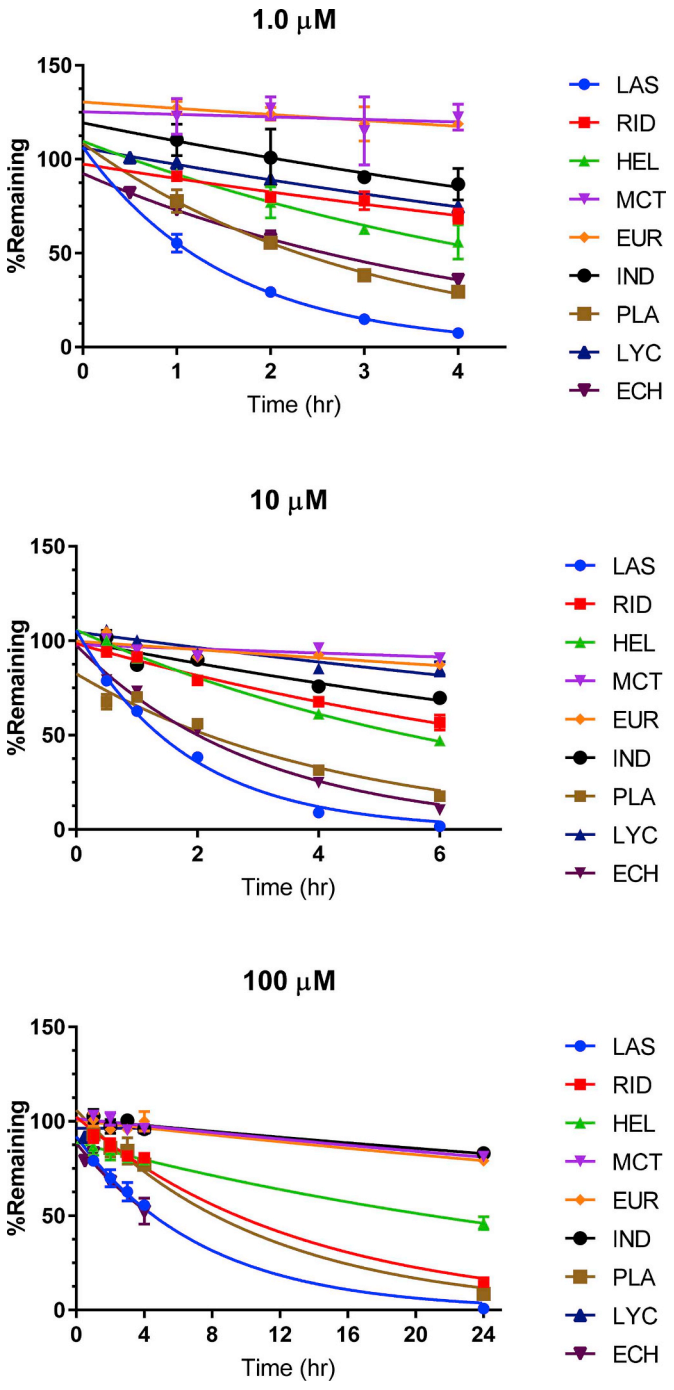

Fig. 3. Time dependent depletion of the parent PA in the culture media of incubations with rat SCHs with a substrate concentration of 1, 10 and 100 μM plotted as mean ± SD for data points acquired in triplicate or mean ± range for data points acquired in duplicate.

Because variability existed among the different studies executed with a 24 h incubation time and 100 μM concentration with one replicate performed per measurement, the data were fit to a mixed effects model after applying a variance-stabilizing square-root transformation. A plot of the model predicted mean adduct counts and associated 95% confidence intervals better illustrates the relative potential for the different PAs to form DHP-DNA adducts under the conditions used and is shown in Fig. 5.

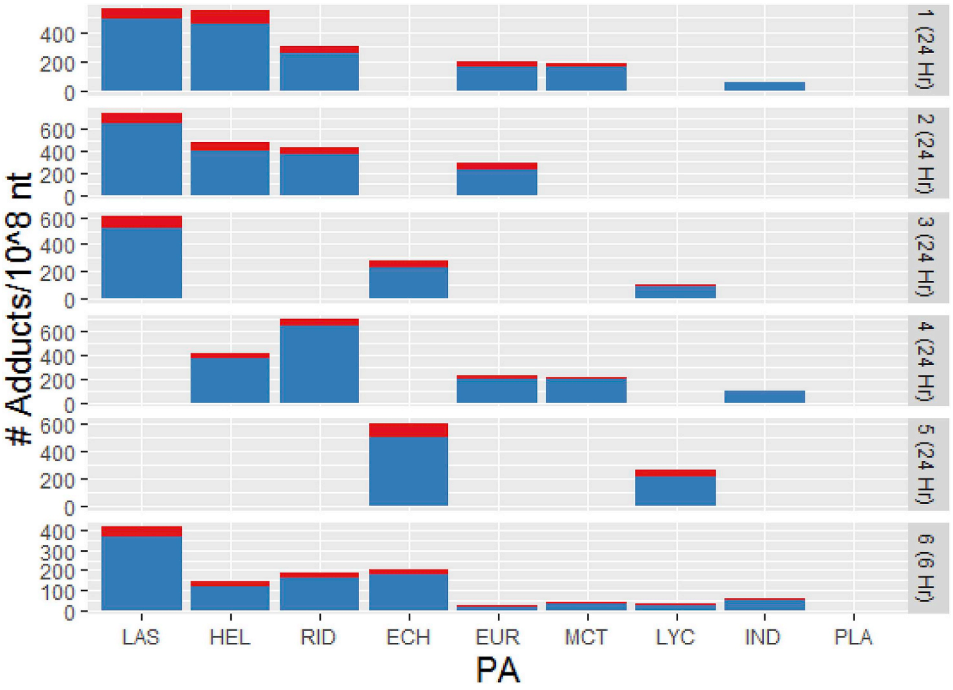

Fig. 4. Levels of DHP-DNA adducts generated for a series of PAs in rat SCHs at a concentration of 100 μM. Total adducts shown equal the sum of DHP-dG-3/4 (blue) and DHP-dA-3/4 (red) adducts/10^8 nucleotides. Each row represents a study performed using hepatocytes isolated from a single rat with incubation time in parentheses. (For interpretation of the references to colour in this figure legend, the reader is referred to the Web version of this article.)

4.4. Dose response of DHP-DNA adduct formation

The dose response of DNA adduct formation was determined by incubating rat SCHs with LAS, RID, HEL or EUR at concentrations of 10, 30 and 100 μM for 24 h. The linear relationship between adduct levels and the AUC for the parent PA in the extracellular media is shown in Fig. 6A for the three concentrations considered. LAS displays the steepest slope corresponding to the greatest number of adducts formed and the lower AUC resulting from faster depletion of parent. RID displays the second highest level of adducts relative to AUC followed by HEL and then EUR which displays the largest AUC for each data point with the lowest adduct levels.

Fig. 6B displays another way of looking at the dose response data by normalizing the total adducts/AUC ratios for RID, HEL and EUR to the ratio for LAS at each concentration tested. The trend for intrinsic relative potency remains consistent and appears to be independent of concentration.

4.5. DHP-DNA adduct levels relative to AUC for depletion of parent in the cellular media

Fig. 7 displays the ratio of total adduct levels to the AUC for the parent PA for the 6 and 24 h incubation times. Model predicted mean values are used for the 24 h adduct levels. It is interesting to note that the adducts/AUC ratio for the two incubation times is close for most PAs and is equal to 1 for LAS which facilitates comparison of the ratios for the remaining PAs relative to LAS. These ratios provide a measure of the potential to form DNA adducts relative to hepatocyte exposure to the parent PA and are displayed in Table 4. The greatest ratio of adducts/AUC is observed for LAS followed by ECH, RID and HEL. Relatively low ratios are generated for EUR, MCT, LYC and IND. Since no adducts were measured for PLA, the ratio is 0 for this PA. Calculated ratios are displayed in Table 4.

5. Discussion

1,2-Unsaturated PAs exhibit a strong structure toxicity relationship. Here we explore this relationship *in vitro* by studying DNA adduct formation and metabolic kinetics in SCH incubations with structurally diverse PAs. Data presented represent some of the first examples of DHP-DNA adduct formation in a fully functional cell model. The accumulation of DNA adducts is complex and controlled by processes including metabolic activation, clearance and DNA repair. The SCH model used here appropriately accounts for the interplay between metabolism and active transport, including excretion into the bile pocket, since all transporter proteins are expressed and properly localized and all phase I and phase II metabolizing enzyme levels are preserved and almost equivalent to those *in vivo* (Swift et al., 2010). While an extensive characterization of intracellular PA concentrations has not been completed in this study we have shown that DNA adduct formation is controlled by the rate and extent of parent chemical depletion and correlates with the AUC of PAs in the cellular medium. DNA adducts, therefore can be considered a surrogate measure of the reactive pyrrolic ester intermediate that forms intracellularly and is PA dependent.

Two pairs of DHP-DNA adducts were measured and are consistent with the epimeric DHP-dG-3/4 and DHP-dA-3/4 adducts detected *in vivo* and *in vitro* in cell systems (Fu et al., 2017; He et al., 2017; Xia et al., 2013; Zhu et al., 2017). No evidence was found of the additional DHP-dG-1/2 or DHP-dA-1/2 pairs of adducts that have been observed in *vitro* in preparations containing rat liver microsomes plus calf thymus DNA (Zhao et al., 2012). All DHP-DNA adducts result from the reaction of electrophilic carbocations formed at the C7 or C9 carbon atom of the reactive DHP ester intermediate with the exocyclic nitrogen of DNA purines. The DHP-dG-1/2 and DHP-dA-1/2 adducts are produced by reaction of the C7 carbon of the DHP ester with deoxyguanosine and deoxyadenosine, while the DHP-dG-3/4 and DHP-dA-3/4 epimers result from reaction of the C9 carbon (Xia et al., 2013). It has been proposed that steric hindrance in the vicinity of the C7 carbon may direct the reaction to preferentially take place at the C9 position, and perhaps the levels of the DHP-dG-1/2 and DHP-dA-1/2 adducts occur to a much lesser extent and below the levels of quantitation for *in vivo* and *in vitro* cellular incubations (Xia et al., 2013). However, no evidence for the formation of DHP-dG-1/2 or DHP-dA-1/2 isomers was generated in the current study even for samples forming the highest adduct levels.

The current work demonstrates that DHP-DNA adduct formation *in vitro* varies linearly with PA concentration. Fig. 6A shows this relationship between AUC and DNA adduct levels for LAS, HEL, RID and

Table 3
DHP-dG and DHP-dA adduct data for 9 PAs as a function of study, concentration and incubation time. ND = not detected. f_m represents the fraction of parent metabolized at the incubation time of the assay.

Chemical Name	Nominal [S] (μM)	Incubation Time (hr)	Study No.	Fraction Metabolized (f_m)	DHP-dA (#adducts/ 10^8 nt)	DHP-dG (#adducts/ 10^8 nt)	Total Adducts (#adducts/ 10^8nt)
Lasiocarpine	10	24	2	1.00	9.4	45.9	55.3
LAS	30	24	2	1.00	29.2	139.3	168.5
	100	24	2	1.00	105.5	640.5	746.0
	100	24	1	0.99	68.4	487.7	556.1
	100	24	3	0.99	89.1	517.6	606.7
	100	6	6	0.62	52.4	364.6	417.0
Riddelliine	10	24	2	0.90	15.5	91.0	106.4
RID	30	24	2	0.86	24.9	180.4	205.3
	100	24	2	0.75	50.8	375.6	426.4
	100	24	1	0.85	47.3	259.2	306.5
	100	24	4	0.81	50.2	641.9	692.1
	100	6	6	0.13	25.4	157.4	182.8
Heliotrine	10	24	2	0.91	12.5	38.7	51.2
HEL	30	24	2	0.70	31.3	122.9	154.2
	100	24	2	0.46	79.5	393.0	472.5
	100	24	1	0.54	92	458.4	550.5
	100	24	4	0.29	41.8	375.4	417.1
	100	6	6	0.31	26.2	113.6	139.8
Europine	10	24	2	0.46	11.1	32.6	43.7
EUR	30	24	2	0.26	30.9	23.0	53.9
	100	24	2	0.22	60.3	230.2	290.6
	100	24	1	0.21	35.5	170.7	206.2
	100	24	4	0.18	21.2	201.4	222.6
	100	6	6	0.36	6.1	16.9	23.0
Monocrotaline	100	24	1	0.19	23.2	164.7	187.9
MCT	100	24	4	0.04	23.2	190.2	213.4
	100	6	6	0.00	5.7	31.6	37.3
Echimidine	100	24	3	0.95	45.1	229.4	274.4
ECH	100	24	5	0.97	98.8	505.3	604.1
	100	6	6	0.55	25.1	180.0	205.1
Indicine	100	24	1	0.17	< 11.1	60.4	60.4
IND	100	24	4	0.24	< 11.1	99.3	99.3
	100	6	6	0.00	5.5	47.1	52.6
Lycopsamine	100	24	3	0.10	18.8	88.2	106.9
LYC	100	24	5	ND	42.7	215.7	258.4
	100	6	6	0.00	7.1	24.1	31.2
Platyphylline	100	24	1	0.92	ND	ND	ND
PLA	100	24	5	0.93	ND	ND	ND

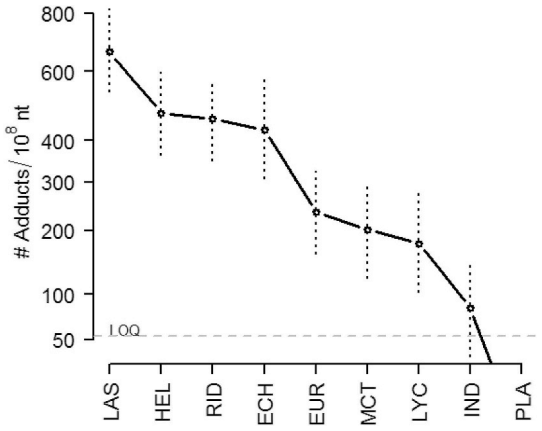

Fig. 5. Model predicted mean total (DHP-dG + DHP-dA) adduct counts (# adducts/10^8nt) and associated 95% confidence intervals for adducts produced in rat SCHs in incubations of 100 μM PA for 24 h (model input data presented in Fig. 3).

EUR. A linear dose-response for DNA adduct formation also was observed *in vivo* in mice for retrorsine (RET) after administration of a single dose and for RID and MCT in female rats dosed for 3 consecutive days (Zhu et al., 2017). Paini et al. (2010) have demonstrated that *in vitro* measurements of DNA adduct formation in rat hepatocytes as a function of metabolite AUC could be used to construct a model capable of correctly predicting *in vivo* levels of adduct formation from estragole in the rat. The authors show that it is possible to model a toxicodynamic endpoint such as DNA adduct formation using only *in vitro* data and in a similar manner it would be possible in our assay to probe adduct formation in the presence of lower PA concentrations by extrapolating the adducts versus AUC curve down to more physiologically relevant amounts.

The intrinsic potencies calculated as adducts/AUC ratio displayed in Fig. 6B for HEL, RID and EUR relative to the ratio for LAS appear to be independent of concentration within the range of doses tested. These data demonstrate that the relative intrinsic potencies measured at these higher concentrations can be expected to be the same at lower physiologically relevant concentrations. This is a conservative assumption since it is likely that DNA repair processes may play a role at low

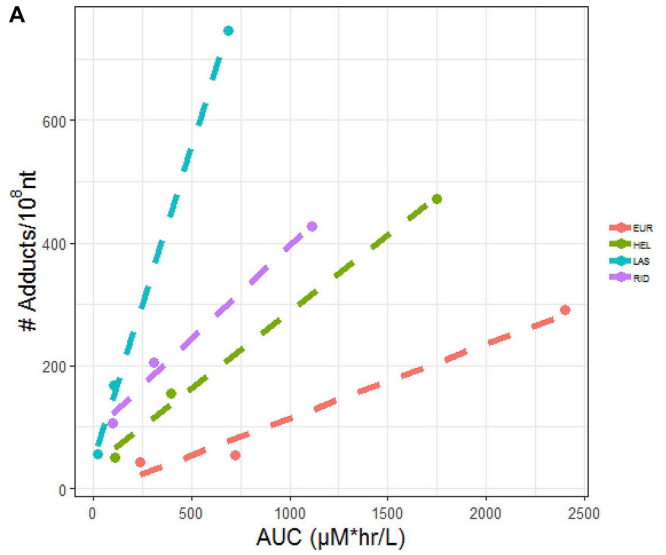

Fig. 6A. Levels of total adducts expressed as # adducts/10^8 nt for 4 PA as a function of *in vitro* AUC (μmol*hr/L) after a 24 h incubation time (data from study #2 in Table 1).

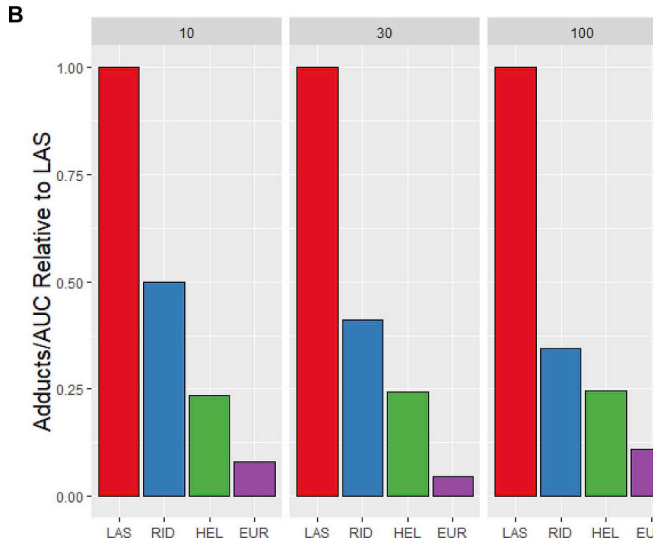

Fig. 6B. Total DHP-DNA adducts (DHP-dG-3/4 + DHP-DA-3/4)/AUC ratios for LAS, RID, HEL and EUR after 24 h incubations as a function of concentration (10, 30, 100 μM) normalized to the #adducts/AUC ratio for LAS.

concentrations, correcting damage prior to replication and ensuring normal cell function.

We propose here that the adducts to AUC ratio (adducts/AUC) provides a measure of the intrinsic hepatic potency of each PA reflecting hepatocyte exposure to DNA reactive metabolites *in vitro*. These ratios are displayed in Table 4 along with the pRPFs proposed by Merz and Schrenk (2016). Our measures of intrinsic potency, like the Merz and Schrenk factors, show that PAs span several orders of magnitude and display the following trend: LAS > ECH ~ RID ~ HEL > EUR ~ MCT ~ LYC ~ IND > PLA. LAS is the most potent PA in our assays displaying an adduct/AUC ratio of 1.0, and the adduct/AUC ratio for HEL for both incubation times is 0.3 in our assays matching the pRPF. RID is a potent cyclic diester and is shown to generate some of the highest adduct levels in this study but has an overall adduct/AUC ratio of 0.4 which is lower than the assigned pRPF of 1.0. EFSA have calculated a $BMDL_{10}$ of 237 μg/kg bw per day for RID derived for the incidence of liver haemangiosarcoma in female rats, whereas a $BMDL_{10}$ of 70 μg/kg bw was derived previously for LAS from a study of limited design for liver haemangiosarcoma in male rats (EFSA, 2017). The data presented here display similar differences to the *in vivo* tumor $BMDL_{10}$ values. Other PAs displaying similar relative potencies to those proposed by Merz and Schrenk include EUR with an adducts/AUC ratio of 0.1 compared to a pRPF of 0.3, and the lower potency PAs IND and LYC which display the lowest adducts/AUC ratios comparable to the lowest pRPFs. The adducts/AUC ratio measured for MCT, however, is much smaller than the pRPF of 1.0. The data presented here demonstrate that MCT is metabolically stable in the rat SCH resulting in very low adduct formation. Also, in contrast to the pRPF, ECH was extensively metabolized and produced an adducts/AUC ratio in our assays higher than the pRPF of 0.1. The trend we have observed in relative adducts/AUC levels compare favorably with the ranking of relative genotoxic potency using micronuclei assessed via flow cytometry in HepaRG cells, where it was shown that the potential to cause DNA damage spanned 3 orders of magnitude for a large series of PAs and their N-oxides (Allemang et al., 2018). Both series of *in vitro* data show a maximum potency for LAS followed by ECH, RID and HEL with lower potencies for EUR, MCT, LYC and IND. In both assays, MCT displayed a much lower and ECH a much higher intrinsic potency than predicted by their proposed pRPFs. The higher intrinsic potency observed for ECH is consistent with other *in vitro* studies in the literature. Significant metabolism-mediated cytotoxicity was shown to occur for both ECH and MCT in a coincubation system containing HepG2/C3A cells with male rat liver S9 fractions (Tamta et al., 2012). However, it is important to note these data reflect only intrinsic potency and do not consider effects resulting from differences in oral absorption and intestinal metabolism with possible active excretion from the gastrointestinal epithelium into the gut lumen, as has been suggested for HEL and ECH (Hessel et al., 2014).

The data also can be compared to findings in another study, where female rats were dosed with a series of PAs for 3 consecutive days (Xia et al., 2013). LAS, RID and MCT were found to generate relatively high levels of DHP-DNA adducts with the following trend for the PAs studied: RET > LAS > RID ~ MCT > RID Nox > Senkirkine (SEK) > HEL ≥ Clivorine (CLI) > LYC ~ retronecine (no ester bonds) ~ PLA. Except for MCT, the observed trend correlates with the intrinsic potencies summarized in Table 4. In this *in vivo* study, MCT was found to generate adduct levels comparable to those for RID, displaying a much higher response than the intrinsic potencies determined here by way of liver cell systems. Several factors may contribute to this difference in response, most significantly that *in vivo* DHP-DNA adducts detected in the liver result from metabolic activation of PAs after oral administration, therefore differences in intestinal permeability and intestinal metabolism also may contribute to relative adduct levels. Notably, levels for hepatic DHP-DNA adducts for RID Nox were found to be lower than for the parent PA because reduction of the N-oxide bond must occur before activation to the reactive pyrrolic ester intermediate. N-oxide bond reduction may occur in the gut or the liver. Additionally, the cell model (male Sprague-Dawley rat hepatocytes used here compared to *in vivo* data in female rats) and dosing (a single dose used here compared to 3 days of dosing *in vivo*) may have played a role, but nonetheless, we observe that the relative levels of adducts correlate well with *in vivo* adduct and tumor potency data, e.g. as reported by Xia (Xia et al., 2013) with a ranking of potential tumor potency as follows: (i) No liver tumor formation (LYC, retronecine), (ii) low liver tumor formation (CLI, HEL), moderate liver tumor formation (MCT) (iv) strong liver tumor formation (RET, LAS, RID, SEK).

Overall, the fraction of reactive metabolites expressed by way of DHP-DNA adducts/AUC considered in this study demonstrate again there is a wide range of relative potencies dependent on PA structures. DHP-DNA adduct levels themselves reflect the intracellular levels of the PAs in the rat SCH model resulting from an interplay of uptake, efflux and biotransformation consisting of both activating and detoxifying events. Using the nominal concentration of PAs in the extracellular media the adduct levels in the cell may be considered relative to the area under the concentration versus time curve (AUC) from which we

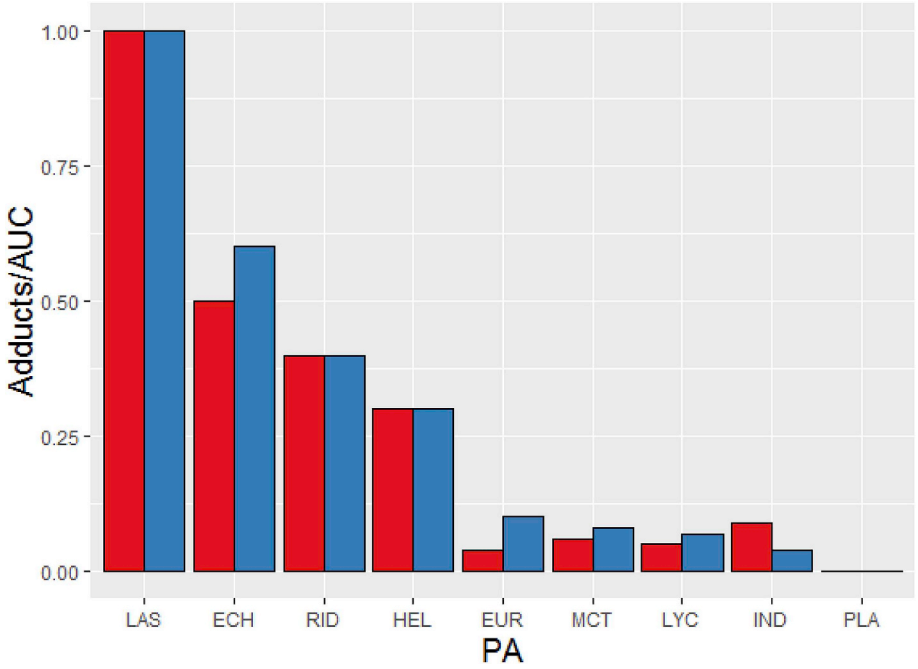

Fig. 7. Total DHP-DNA adducts (DHP-dG-3/4 + DHP-dA-3/4)/AUC for incubations containing a PA concentration of 100 μM for 6 h (red) or 24 h (blue). Model-predicted mean levels are used for the 24 h adduct data. (For interpretation of the references to colour in this figure legend, the reader is referred to the Web version of this article.)

Table 4
Adducts/AUC ratio for all PAs in this study after 6 and 24 h incubations in comparison with the pRPFs developed by Merz and Schrenk (2016). Model-predicted mean adduct levels were used for the 24 h adduct levels.

Chemical Name	Model-Predicted Mean # Adducts (24 h)	# Total Adducts/AUC (6 h) #Adducts*μmol*hr/10^8nt*L	# Total Adducts/AUC (24 h) # Adducts*μmol*hr/10^8nt*L	pRPF Merz and Schrenk
Lasiocarpine LAS	663	1.0	1.0	1.0
Heliotrin HEL	475	0.3	0.3	0.3
Riddelliine RID	459	0.4	0.4	1.0
Echimidine ECH	428	0.5	0.7	0.1
Europine EUR	236	0.04	0.1	0.3
Indicine IND	84	0.09	0.04	0.01
Monocrotaline MCT	202	0.06	0.09	1.0
Lycopsamine LYC	177	0.05	0.08	0.01
Platyphylline PLA	–	0.0	0.0	0.0

see an intrinsic potency ranking as follows: LAS > ECH ~ RID ~ HEL > EUR ~ MCT ~ LYC ~ IND under the experimental conditions performed here. This approach accounts for differences in adduct levels resulting from substrate depletion over the course of the incubation and thus reflects the central role of liver cell metabolism.

6. Conclusion

In conclusion, we have shown through a biologically relevant *in vitro* testing approach that the rate and extent of metabolic activation is critical to the differing potencies of PAs. This study provides a central piece of evidence that, as Merz and Schrenk first suggested, PAs can be distinguished on a potency basis. Relative levels of DHP-DNA adducts as a function of the kinetics of PA metabolism provide an input to the assessment of the relative toxic potencies of the PAs. With a better understanding of toxicokinetics, potency factors may eventually be derived and applied in risk assessment.

Acknowledgments

We wish to thank Bastian Selman for generating the dose-response curves and Corie Ellison for his suggestions and technical review of the manuscript. This work was funded by Procter & Gamble, by whom the authors are employed.

Transparency document

Transparency document related to this article can be found online at https://doi.org/10.1016/j.fct.2019.05.031.

References

Allemang, A., Mahony, C., Lester, C., Pfuhler, S., 2018. Relative potency of fifteen pyrrolizidine alkaloids to induce DNA damage as measured by micronucleus induction in HepaRG human liver cells. Food Chem. Toxicol. 121, 72–81.
Bates, D., Mächler, M., Bolker, B., Walker, S., 2015. Fitting Linear Mixed-Effects Models Using Lme4, vol. 67. pp. 48 2015.
EFSA, 2011. Scientific Opinion on Pyrrolizidine alkaloids in food and feed. EFSA Journal 9, 2406.
EFSA, 2017. Risks for human health related to the presence of pyrrolizidine alkaloids in honey, tea, herbal infusions and food supplements. EFSA Journal 15, 4908.
Fu, P.P., 2017. Pyrrolizidine alkaloids: metabolic activation pathways leading to liver tumor initiation. Chem. Res. Toxicol. 30, 81.
Fu, P.P., Xia, Q., He, X., Barel, S., Edery, N., Beland, F.A., Shimshoni, J.A., 2017. Detection of pyrrolizidine alkaloid DNA adducts in livers of cattle poisoned with Heliotropium europaeum. Chem. Res. Toxicol. 30, 851–858.
Fu, P.P., Xia, Q., Lin, G., Chou, M.W., 2004. Pyrrolizidine alkaloids–genotoxicity, metabolism enzymes, metabolic activation, and mechanisms. Drug Metab. Rev. 36, 1–55.
He, X., Xia, Q., Fu, P.P., 2017. 7-glutathione-pyrrole and 7-cysteine-pyrrole are potential carcinogenic metabolites of pyrrolizidine alkaloids. J. Environ. .Sci. Health. C 1–15.
He, X., Xia, Q., Ma, L., Fu, P.P., 2016. 7-cysteine-pyrrole conjugate: a new potential DNA reactive metabolite of pyrrolizidine alkaloids. J. Environ. .Sci. Health. C 34, 57–76.
He, X., Xia, Q., Wu, Q., Tolleson, W.H., Lin, G., Fu, P.P., 2019. Primary and secondary pyrrolic metabolites of pyrrolizidine alkaloids form DNA adducts in human A549 cells. Toxicol. Vitro 54, 286–294.

Hessel, S., Gottschalk, C., Schumann, D., These, A., Preiss-Weigert, A., Lampen, A., 2014. Structure-activity relationship in the passage of different pyrrolizidine alkaloids through the gastrointestinal barrier: ABCB1 excretes heliotrine and echimidine. Mol. Nutr. Food Res. 58, 995–1004.

Lame, M.W., Jones, A.D., Morin, D., Segall, H.J., Wilson, D.W., 1995. Biliary excretion of pyrrolic metabolites of [14C]monocrotaline in the rat. Drug Metab. Dispos. 23, 422–429.

Manchester, K.L., 1995. Value of A260/A280 ratios for measurement of purity of nucleic acids. Biotechniques 19, 208–210.

Merz, K.H., Schrenk, D., 2016. Interim relative potency factors for the toxicological risk assessment of pyrrolizidine alkaloids in food and herbal medicines. Toxicol. Lett. 263, 44–57.

Obach, R.S., 1999. Prediction of human clearance of twenty-nine drugs from hepatic microsomal intrinsic clearance data: an examination of in vitro half-life approach and nonspecific binding to microsomes. Drug Metab. Dispos. 27, 1350–1359.

Paini, A., Punt, A., Viton, F., Scholz, G., Delatour, T., Marin-Kuan, M., Schilter, B., van Bladeren, P.J., Rietjens, I.M.C.M., 2010. A physiologically based biodynamic (PBBD) model for estragole DNA binding in rat liver based on in vitro kinetic data and estragole DNA adduct formation in primary hepatocytes. Toxicol. Appl. Pharmacol. 245, 57–66.

Ruan, J., Liao, C., Ye, Y., Lin, G., 2014a. Lack of metabolic activation and predominant formation of an excreted metabolite of nontoxic platynecine-type pyrrolizidine alkaloids. Chem. Res. Toxicol. 27, 7–16.

Ruan, J., Yang, M., Fu, P., Ye, Y., Lin, G., 2014b. Metabolic activation of pyrrolizidine alkaloids: insights into the structural and enzymatic basis. Chem. Res. Toxicol. 27, 1030–1039.

Swift, B., Pfeifer*, N.D., Brouwer, K.L.R., 2010. Sandwich-cultured hepatocytes: an in vitro model to evaluate hepatobiliary transporter-based drug interactions and hepatotoxicity. Drug Metab. Rev. 42, 446–471.

Tamta, H., Pawar, R.S., Wamer, W.G., Grundel, E., Krynitsky, A.J., Rader, J.I., 2012. Comparison of metabolism-mediated effects of pyrrolizidine alkaloids in a HepG2/C3A cell-S9 co-incubation system and quantification of their glutathione conjugates. Xenobiotica 42, 1038–1048.

Tu, M., Li, L., Lei, H., Ma, Z., Chen, Z., Sun, S., Xu, S., Zhou, H., Zeng, S., Jiang, H., 2014. Involvement of organic cation transporter 1 and CYP3A4 in retrorsine-induced toxicity. Toxicology 322, 34–42.

Tu, M., Sun, S., Wang, K., Peng, X., Wang, R., Li, L., Zeng, S., Zhou, H., Jiang, H., 2013. Organic cation transporter 1 mediates the uptake of monocrotaline and plays an important role in its hepatotoxicity. Toxicology 311, 225–230.

Xia, Q., He, X., Ma, L., Chen, S., Fu, P.P., 2018. Pyrrolizidine alkaloid secondary pyrrolic metabolites construct multiple activation pathways leading to DNA adduct formation and potential liver tumor initiation. Chem. Res. Toxicol. 31, 619–628.

Xia, Q., Zhao, Y., Von Tungeln, L.S., Doerge, D.R., Lin, G., Cai, L., Fu, P.P., 2013. Pyrrolizidine alkaloid-derived DNA adducts as a common biological biomarker of pyrrolizidine alkaloid-induced tumorigenicity. Chem. Res. Toxicol. 26, 1384–1396.

Zhao, Y., Xia, Q., Gamboa da Costa, G., Yu, H., Cai, L., Fu, P.P., 2012. Full structure assignments of pyrrolizidine alkaloid DNA adducts and mechanism of tumor initiation. Chem. Res. Toxicol. 25, 1985–1996.

Zhu, L., Xue, J., Xia, Q., Fu, P.P., Lin, G., 2017. The long persistence of pyrrolizidine alkaloid-derived DNA adducts in vivo: kinetic study following single and multiple exposures in male ICR mice. Arch. Toxicol. 91, 949–965.